mater.scichina.com link.springer.com https://doi.org/10.1007/s40843-025-4000-1

Green solvent engineering and additive modulation in stabilized black $FAPbI_3$ perovskite single crystals for high-performance photodetectors

Meitong Guo[1†], Ying Wang[2†*], Binyi Zhou[1], Siyv Li[2], Bingbing Zhang[2], Hongbo Huang[2], Zhenguang Wang[2], Leipeng Li[1,3*], Shufang Wang[1], Linjuan Guo[1], Caofeng Pan[4*] and Zheng Yang[1,3*]

ABSTRACT **Formamidine lead-based perovskites ($FAPbI_3$) exhibit significant potential in optoelectronic applications. Nevertheless, they encounter challenges related to δ-phase instability and reliance on toxic solvents. In this study, we present a green solvent-additive synergy strategy that employs γ-valerolactone (GVL) in conjunction with reductive acids like oxalic acid (OA), to stabilize α-$FAPbI_3$ single crystals (SCs). GVL enhances the stability of the precursors through the formation of FA^+-GVL hydrogen bonds and high-valence $[PbI_x]^{2-x}$ clusters, resulting in ambient-stable α-phase SCs, yielding a marked improvement in stability compared to SCs prepared with the toxic solvent γ-butyrolactone (GBL). Additive modulation demonstrates that H^+ and reductive groups play a critical role in regulating crystallization, suppressing the δ-phase by promoting FA^+ dissociation and inhibiting MA^+ deprotonation. A solvent-involved intermediate, δ-$FAPbI_3$-GVL, has been identified; this intermediate evolves into α-$FAPbI_3$ at a low temperature of 60 °C, thereby reducing the energy barriers associated with the α to δ phase transition. In contrast, non-reductive acids and reductive ionic liquids do not inhibit δ-phase formation, with the latter even promoting the crystallization of pure δ-$FAPbI_3$. By utilizing low-volatility OA as an additive, optimized $FA_{0.9}MA_{0.1}PbI_3$ single crystal thin films exhibit a low defect density of 8.3×10^{11} cm^{-3}. Subsequently, a photodetector was fabricated. Under zero bias voltage and 780 nm illumination, the device exhibited a responsivity of 14.5 mA/W, a detectivity of 3.75×10^{10} Jones, and a response speed of 149/65 μs. Moreover, without any encapsulation, the device's performance diminished by only 17% after 30 days of storage in ambient conditions, indicating remarkable stability.**

Keywords: $FAPbI_3$, green solvent engineering, solvent-involved intermediate, additive modulation, photodetector

INTRODUCTION

Metal halide perovskites (MHPs) have emerged as promising candidates for photovoltaic and optoelectronic devices [1–5] due to their exceptional light absorption coefficients, long carrier diffusion lengths, tunable band gaps, and low defect densities [6–9]. While most MHP-based photodetectors (PDs) currently utilize polycrystalline thin films, their performance and stability are significantly hindered by the presence of amorphous or low-crystallinity grain boundaries [10–15]. In contrast, MHP single-crystal (SC) films exhibit superior optoelectronic characteristics owing to their grain-boundary-free structure [16–18]. Formamidinium lead triiodide ($FAPbI_3$) perovskites, which possess enhanced optoelectronic properties and greater thermal stability compared to $MAPbI_3$, are regarded as ideal candidates for high-efficiency optoelectronics [19–22]. Nonetheless, the spontaneous α-to-δ phase transition at ambient conditions, induced by the lattice distortion resulting from the large ionic radius of FA^+ (2.79 Å), poses a significant challenge for their practical application [18,23,24].

Recent advances in compositional engineering, such as MA^+/Cs^+ doping [25–30], and additive modulation using MAAc or formic acid (Fa) [31–39], have partially mitigated phase instability. Progress has also been achieved in improving the overall stability of perovskite optoelectronic devices through strategies like interface engineering and defect passivation [40,41]. Nevertheless, these methods still depend on the use of toxic or flammable solvents like γ-butyrolactone (GBL) or 2-methoxyethanol (2-ME), which hinder scalability and environmental friendliness. GBL is known for its toxicity and its tendency to hasten phase degradation due to residue buildup [42], whereas flammable 2-ME only yields microcrystalline powders instead of SCs [43,44]. γ-valerolactone (GVL), a green solvent derived from lignocellulosic biomass, provides eco-friendly processing, cost-effectiveness, and food-grade safety [45–50]. However, the crystallization mechanisms that govern δ-phase suppression in green solvent systems remain poorly understood, which impedes rational material design. Chu *et al.* [46] demonstrated the growth of δ-$FAPbI_3$ SC using GVL as the solvent. In contrast, α-$FAPbI_3$ SCs can only be obtained at elevated growth or annealing temperatures. A systematic investigation into the growth and crystallization mechanisms of black-phase perovskites, such as α-$FAPbI_3$, in GVL under low-temperature conditions is essential for elucidating the thermodynamic and kinetic pathways that govern phase-pure

[1] Hebei Key Laboratory of Photo-Electricity Information and Materials, College of Physics Science and Technology, Hebei University, Baoding 071002, China
[2] College of Chemistry and Materials Science, Key Laboratory of Medicinal Chemistry and Molecular Diagnosis of the Ministry of Education, Hebei Research Center of the Basic Discipline of Synthetic Chemistry, Key Laboratory of Chemical Biology of Hebei Province, Hebei University, Baoding 071002, China
[3] Institute of Life Science and Green Development, Hebei University, Baoding 071002, China
[4] Institute of Atomic Manufacturing, Beihang University, Beijing 100191, China
[†] Equally contributed to this work.
[*] Corresponding author (email: wangy@hbu.edu.cn; lpl@hbu.edu.cn; pancaofeng@buaa.edu.cn; yangzheng06@hbu.edu.cn)

formation.

We present a comprehensive study addressing the challenges of δ-phase instability and solvent toxicity in $FAPbI_3$ perovskites. By combining green solvent engineering with additive modulation, we elucidate the crystallization mechanisms governing α-phase stabilization. Through *in situ* characterization and additive functionality screening, we identify a solvent-involved intermediate (δ-$FAPbI_3$-GVL) that promotes low-energy α-phase formation at 60 °C, overcoming thermodynamic and kinetic limitations of conventional systems. Additionally, optimizing the composition ($FA_{0.9}MA_{0.1}PbI_3$) and using reductive acid additives to achieve single crystal thin film (SCTF) with minimal defect densities result in photodetectors with high responsivity (14.5 mA/W) and environmental durability (83% performance retention over 30 days). This study not only clarifies the roles of solvent-additive interactions in phase control but also establishes a scalable green synthesis approach for stable MHP optoelectronics.

RESULTS AND DISCUSSION

Precursor solutions were prepared with GBL and GVL solvents, and $FAPbI_3$ perovskite single crystals were grown via reverse temperature crystallization (Fig. S1). The powder X-ray diffraction (XRD) analysis in Fig. 1a indicates that $FAPbI_3$ crystals synthesized using different precursor solvents exhibit the δ-$FAPbI_3$ structure. Notably, black single crystals based on GBL completely changed to yellow crystals after 3 days in a desiccator, while GVL-based crystals remained black. GVL-based crystals demonstrated superior crystal stability compared to GBL-based ones (Fig. 1b). Further analyses reveal the enhanced stability of GVL-based crystals. In Fig. 1c, d, the Fourier transform infrared (FTIR) spectra of the GVL-$FAPbI_3$ solution, in contrast to pure GVL solvent, displayed an N–H stretching vibration of FA^+ at 3370 cm^{-1}, with a slight redshift and splitting of the C=O bond at 1761 cm^{-1}. This suggests hydrogen bonding between C=O and FA^+, leading to reduced electron density on O and a lower C=O vibration frequency. The Fermi resonance between C=O and FA^+ (N–H) induced peak splitting. Such interactions were absent in GBL (Fig. S2). Ultraviolet-visible (UV-vis) absorption spectra in Fig. S3 exhibited a prominent 300 nm peak in GVL-FAI, confirming strong GVL-FA^+ interactions. The poor solubility of PbI_2 in GVL alone indicated minimal interaction between GVL and PbI_2 (Fig. S4).

Studies indicate that perovskite precursors form $[PbI_x]^{2-x}$ complexes in solution [49], and their valence states significantly impact solution stability and crystallization. As illustrated in Fig. 1e, the GVL-$FAPbI_3$ solution exhibits a notable redshift compared to GBL-$FAPbI_3$, suggesting the presence of higher-valence $[PbI_x]^{2-x}$ species in GVL. Dynamic light scattering (DLS) measurements further demonstrate that the colloidal sizes in GVL-based precursors are larger, supporting the existence of higher-valence $[PbI_x]^{2-x}$ (Fig. 1f). The strong interactions between GVL-FA^+, along with the elevated valence of $[PbI_x]^{2-x}$, collectively enhance the stability of perovskite precursors.

Orange SCs form at 65 °C in GVL-$FAPbI_3$ solution and gradually darken as the temperature increases (Fig. S1). Upon removal from the solution and subsequent heating in air, the orange crystals undergo a phase transition to α-phase crystals, black crystals begin to appear at 60 °C and completely transform into the black phase at 100 °C. In contrast, pure δ-$FAPbI_3$ does not exhibit this behavior (Fig. 2a and Fig. S5). Analysis of the ^1H nuclear magnetic resonance (^1H NMR) spectrum of the washed orange crystals reveals the presence of the –CH peak of GVL (Fig. 2b). The C=O group of the GVL molecule participates in weak hydrogen bonding interactions with FA^+ present in the perovskite lattice. These interactions not only influence the growth of the crystals but also, after crystal formation, may function to "anchor" specific GVL molecules at designated sites

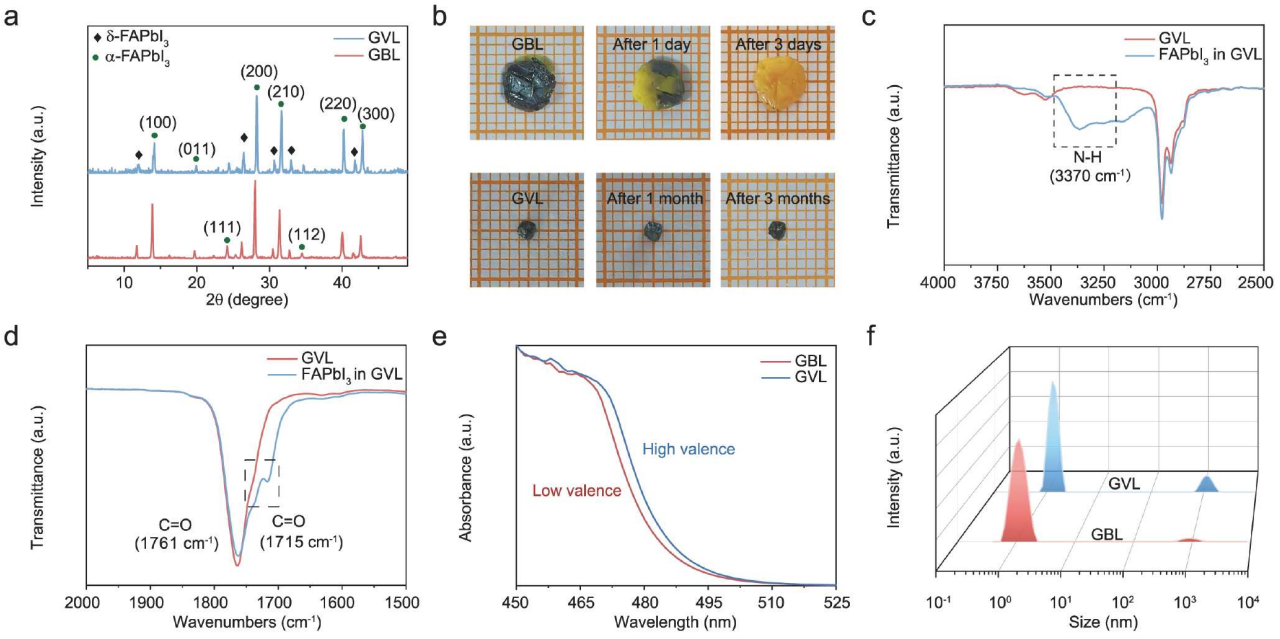

Figure 1 Characterizations of $FAPbI_3$ SCs prepared using GVL and GBL as solvents. (a) XRD patterns of $FAPbI_3$ crystalline powders grown in GVL and GBL. (b) Ambient stability comparison of black $FAPbI_3$ SCs obtained using GVL and GBL solvent systems over 3 months. FTIR spectral analysis: (c) pure GVL solvent and (d) $FAPbI_3$ dissolved in GVL, highlighting FA^+ N–H stretching (3370 cm^{-1}) and C=O bond redshift/splitting (1761 cm^{-1}). (e) UV-vis absorption spectra of GVL and GBL precursor solutions. (f) DLS particle size distributions of GVL and GBL precursors.

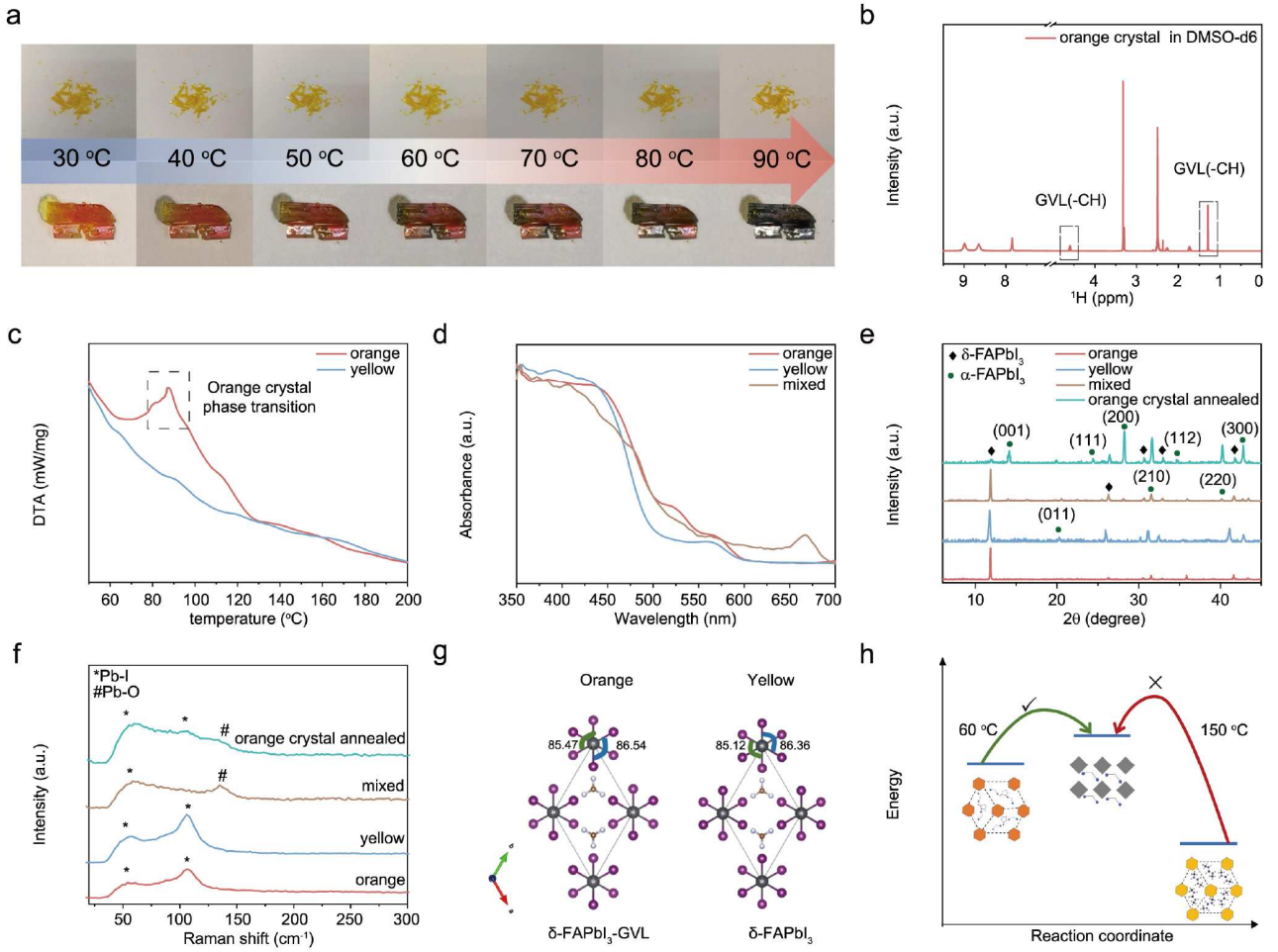

Figure 2 Phase evolution of $FAPbI_3$ with temperature. (a) Structural transition from yellow and orange SCs to α-phase (black) ones upon annealing. (b) ^1H NMR analysis of the washed orange crystals dissolved in DMSO-d6, confirming GVL incorporation. (c) DSC profile (60–200 °C) of yellow and orange crystals, showing a phase change process for orange crystals. (d) UV-vis absorption spectra of as-prepared orange, yellow, and mixed crystals. (e) XRD patterns and (f) Raman spectra of orange, yellow, mixed crystals, and orange crystals after annealing treatment. (g) Structures and I–Pb–I bond angles of different PbI_6 octahedral species, showing that the orange and yellow crystals (δ-phase crystals) belong to the same crystal structure. (h) A reaction scheme to qualitatively illustrate the kinetic control mechanism for the formation of α-$FAPbI_3$ from δ-$FAPbI_3$-GVL or δ-$FAPbI_3$.

on the crystal surfaces or within subsurface regions. Differential scanning calorimetry (DSC) reveals weight loss of orange crystals between 65 and 100 °C, confirming their identity as a solvent compound (Fig. 2c), consistent with the findings in Fig. 2a. In the investigation of the crystallization mechanism of $FAPbI_3$ in GVL, we examined the crystals in different states. The crystal structures of both yellow and orange SCs were determined and refined through SC XRD analysis. Fig. 2d, f demonstrate that orange crystals and δ-$FAPbI_3$ share similar optical absorption, crystal structure, and Pb–I vibration. "Mixed" refers to the composite crystals containing both yellow and black phases, while "orange crystal annealed" indicates α-phase crystals formed the annealed orange crystals in air. In Fig. 2e, orange crystals display a slight shift to higher or lower angles in XRD peak positions and narrower full width at half maximum (FWHM) compared to δ-$FAPbI_3$, suggesting a similar hexagonal crystal structure but potentially reduced strain or larger crystallite size, which is very similar to δ-$FAPbI_3$.

In contrast to the previously reported solvent-containing $FAPbI_3$-based intermediate structures [51], which exhibit a crystal structure markedly different from both α-$FAPbI_3$ or δ-$FAPbI_3$, the incorporation of GVL does not alter the structure of the $FAPbI_3$-based intermediate. Consequently, we hypothesize that GVL molecules occupy the vacancies within the $[PbI_6]^{4-}$ octahedral framework in δ-$FAPbI_3$ crystals. Nevertheless, GVL solvent molecules mitigate lattice distortion in $FAPbI_3$ and promote the formation of α-$FAPbI_3$. The orange-phase crystals were derived from three independently prepared batches, with their initial masses accurately measured using an electronic balance. Subsequently, the crystals underwent isothermal heating at 90 °C for 20 min on a hot stage, leading to a complete transformation into the α-$FAPbI_3$ phase. Post-heating, the masses were re-measured, with the results detailed in Table S1. The variable mass loss observed among the different batches suggests non-stoichiometric GVL content within these crystals. This observation, in conjunction with the similar densities between the orange phase (δ-$FAPbI_3$-GVL) and the pure δ-phase (Table S2), supports the conclusion that the two phases share essentially identical crystalline frameworks. The slight density variation can be ascribed to the flexible integration of GVL molecules into lattice vacancies or channels, thereby fine-tuning the overall density without altering the fundamental crystal

structure. Through comprehensive characterizations, the orange crystal is identified as a solvent-involved complex, δ-$FAPbI_3$-GVL. The proposed structure is illustrated in Fig. 2g, with detailed lattice parameters listed in Tables S2–S8.

Based on the characterization presented, we suggest that at lower temperatures, a strong hydrogen bond forms between the C=O of GVL and FA^+ in the precursor solution. This interaction enhances the solubility of the precursor and facilitates an orderly assembly process. As the temperature increases slightly, the first precipitate observed is not the α-phase but the intermediate δ-$FAPbI_3$-GVL. In this intermediate, GVL is not merely adsorbed; it engages in hydrogen bonding with FA^+ and occupies gaps within the one-dimensional chain-like $[PbI_6]^{4-}$ structure of the δ-phase. This interaction alleviates the lattice distortion induced by the large ionic radius of FA^+, thus reducing the activation energy necessary for α-phase formation. The presence of δ-$FAPbI_3$-GVL shortens the transition pathway from the δ-phase to the α-phase. In contrast to the high-energy direct transition from the δ-phase to α-phase, the stepwise conversion via this intermediate (Fig. 2h) significantly decreases the activation energy, rendering the α-phase thermodynamically favorable at lower temperatures.

Upon further heating, the C=O bond of GVL establishes a Pb–O coordination bond with Pb^{2+}. This interaction disrupts the original δ-phase or disordered precursor structure, thereby facilitating the reconnection of $[PbI_6]$ octahedra. Furthermore, Pb–O bonding secures GVL at the growth interface, directing $[PbI_6]$ octahedra toward a three-dimensional network configuration. Concurrently, as the GVL-FA^+ hydrogen bond dissociates, FA^+ can be incorporated into the voids of the three-dimensional framework formed by $[PbI_6]$ octahedra, guided by the Pb–O bond. Subsequently, some GVL molecules may detach from their anchored positions, enabling I^- to occupy these sites and complete the final $[PbI_6]^{4-}$ coordination. In summary, GVL synergistically lowers both the thermodynamic barrier and kinetic hindrance associated with α-phase formation through two mechanisms: solvation complexation and intermediate regulation. This process facilitates the low-temperature growth of stable α-$FAPbI_3$ SC.

The use of GVL as a solvent improves the crystal stability of $FAPbI_3$ relative to GBL; however, residual δ-phase impurities remain. Current approaches to mitigate δ-phase formation predominantly involve compositional engineering and additive optimization. In this study, we introduced small-sized methylammonium (MA^+) cations into the $FAPbI_3$ lattice, utilizing GVL as the solvent to synthesize $FA_{0.9}MA_{0.1}PbI_3$ SCs, as detailed in Fig. S6. Nonetheless, XRD analysis confirmed the persistent presence of the δ-phase in the resulting crystals (Fig. S7). Further characterization of the precursor solution using UV-vis absorption spectroscopy, FTIR, and DLS indicated that the incorporation of MA^+ cations did not adversely affect the optical properties or colloidal stability of the system. Based on these results, $FA_{0.9}MA_{0.1}PbI_3$ was chosen as the primary focus for subsequent investigations.

This study utilized three categories of additives for δ-phase modulation: (1) reductive ionic liquids, including methylammonium formate (MAFa), dimethylammonium formate (DMAFa), formamidinium formate (FAFa), and methylammonium acetate (MAAc); (2) non-reductive acids, comprising acetic acid (AA), propionic acid (PA), valeric acid (VA), and hexanoic acid (HA); and (3) reductive acids, which consist of hypophosphorous acid (HPA), oxalic acid (OA), citric acid (CA), L-ascorbic acid (L-AA), and Fa.

Crystal growth observations and XRD characterization demonstrate that the incorporation of reductive ionic liquids as additives exclusively results in the formation of yellow-phase crystals (Figs S8 and S9). In contrast, systems utilizing non-reductive acid additives (Figs S10 and S11) continue to display residual yellow-phase crystals. Importantly, the addition of reductive acid additives (Figs S12 and S13) facilitates the successful growth of α-$FA_{0.9}MA_{0.1}PbI_3$. This finding underscores the essential synergistic role of hydrogen ions (H^+) and reductive groups in suppressing δ-phase formation. To elucidate the underlying mechanism, four systems—Control, MAFa, OA, and HA—were selected for a comparative mechanistic study. UV-vis absorption spectra (Fig. 3c) indicate no significant shift in the absorption edge of HA compared to the control. In contrast, OA exhibits a notable red shift, which suggests the presence of higher-coordination Pb–I octahedral structures, while MAFa displays a distinct blue shift. DLS analysis further shows that MAFa reduces the presence of micron-scale nucleation sites, whereas OA significantly increases their abundance (Fig. 3d). Optical microscopy (Fig. S14) confirms that these micron-scale grain seeds serve as effective nucleation sites for the preferential growth of the α-phase. FTIR spectroscopy provides molecular-level evidence of the inhibited interaction between FA^+ and GVL, as evidenced by the disappearance of the characteristic C=N peak at 1716 cm^{-1} in the MAFa system (Fig. 3e). ^1H NMR analysis reveals that, compared to the control device, both HA and OA induce more pronounced peak splitting of the FA^+ (=NH) signal.

This finding suggests that H^+ promotes the dissociation equilibrium of FAI, leading to the generation of free FA^+ and I^-. The resulting FA^+ forms a hydrogen-bonded solvation complex, δ-$FAPbI_3$-GVL, which facilitates the formation of the α-phase perovskite. In systems lacking an external H^+ source (e.g., those with MAFa addition), MA^+ undergoes deprotonation to yield MA^0, which subsequently reacts with FA^+ through nucleophilic interaction to produce methyl formamidinium (MFA^+). The corresponding ^1H peak positions for FA^+ and MFA^+ are illustrated in Fig. S15. Prior studies have confirmed that MFA^+ preferentially coordinates with lead-iodide octahedra [52–54], ultimately resulting in the formation of yellow-phase $MFAPbI_3$ crystals (Fig. 3f, g). Characteristic peaks of dimethylformamidinium ($DMFA^+$) are prominently observed in the ^1H NMR spectrum of the Control (Fig. 3g). The intensity of these peaks is significantly diminished by HA and entirely eliminated by the reductive acid OA. This phenomenon is attributed to the H^+ derived from the additive, which simultaneously enhances the dissociation of FAI while inhibiting the deprotonation of MA^+. However, the consumption of H^+ through I^- oxidation in solution can facilitate the generation of MA^0. Theoretical analysis indicates that the introduction of reductive functional groups effectively mitigates I^- oxidation, thereby completely preventing deprotonation of MA^+. This dual suppression mechanism inhibits the formation of both MFA^+ and $DMFA^+$, thereby achieving complete inhibition of the δ-phase through the following reaction pathways:

$$FAI \rightleftharpoons FA^+ + I^-, \quad (1)$$

$$MA^+ \rightleftharpoons MA^0 + H^+, \quad (2)$$

$$MA^0 + FA^+ \rightarrow MFA^+/DMFA^+, \quad (3)$$

$$4I^- + O_2 + 4H^+ \rightarrow 4I^0 + 2H_2O, \quad (4)$$

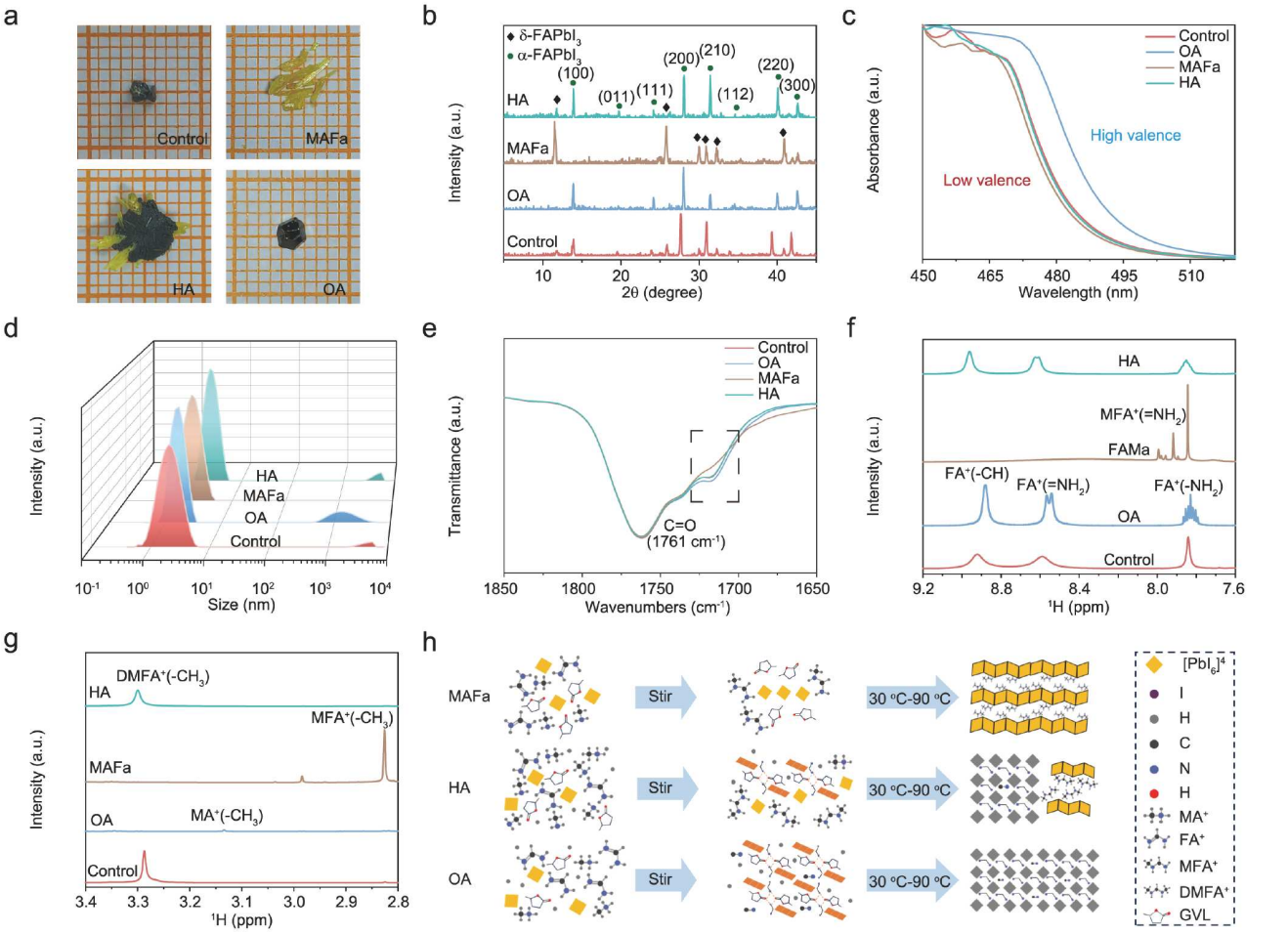

Figure 3 Additive-modulated crystallization kinetics. (a) $FAPbI_3$ SCs grown with different additives. (b) Powder XRD patterns of $FAPbI_3$ SCs synthesized with different additives. (c) UV-vis absorption spectra of precursor solutions added with different additives. (d) DLS of colloidal size distribution analysis of additive-engineered perovskite precursor solutions. (e) Additive-dependent FTIR analysis of precursor solutions. (f, g) ^{1}H NMR spectra of additive-modified perovskite precursor solutions. (h) Mechanism of δ-phase suppression: H^+ promotes FA^+ dissociation; reductive groups inhibit MA^+ deprotonation.

$$HCOO^- + 2I^0 \rightarrow 2I^- + H^+ + CO_2. \quad (5)$$

The synergistic mechanism involving H^+ and reductive groups is illustrated in Fig. 3h. When MAFa is employed as an additive without an external H^+ source, the H^+ necessary for FAI decoupling is supplied by MA^+. After deprotonation, the MA^0 undergoes an irreversible nucleophilic reaction with FA^+ to yield MFA^+. Although the reductive groups in MAFa inhibit I^- oxidation, MFA^+ subsequently interacts with Pb–I octahedra during nucleation, resulting in the formation of the δ-phase. HA additives supply additional H^+ ions, hindering MA^+ deprotonation but failing to prevent I^- oxidation due to the absence of reductive groups. The consumed H^+ in the oxidation process necessitates replenishment through MA^+ deprotonation. The surplus deprotonated MA^0 engages in nucleophilic reaction with FA^+ to generate $DMFA^+$, which interacts with Pb–I octahedra to produce the δ-phase, while any remaining FA^+ combines with Pb–I octahedra to form the α-phase. When OA is utilized as an additive, it offers both H^+ ions and reductive groups concurrently, leading to synergistic effects that impede both MA^+ deprotonation and I^- oxidation, facilitating the production of α-phase SCs. The absence of the δ-phase in $FA_xMA_{1-x}PbI_3$ SCs cultivated in GVL with OA as the additive, as illustrated in Fig. S16, underscores the crystals' compositional adjustability.

The results indicate that the combination of GVL and reductive acidic additives effectively stabilizes α-$FAPbI_3$ SCs. The Fa is a commonly used additive; however, its high volatility, with a boiling point of approximately 100 °C, renders it susceptible to loss during the heating process. Consequently, $FA_{0.9}MA_{0.1}PbI_3$ SCTFs were synthesized using non-volatile OA and volatile Fa as additives (Fig. 4a and Fig. S17). XRD analysis confirmed that the SCTFs grown with OA as the additive were devoid of the δ-phase. In contrast, SCTFs grown with formic acid as the additive exhibited the presence of the δ-phase, attributable to the rapid volatilization of Fa (Fig. 4b). The SCTFs grown with different additives underwent 30 days of ambient storage before XRD analysis. Fig. S18 illustrates that the SCTF incorporating OA as the additive remained phase-stable post-storage, while the SCTF with the Fa additive exhibited intensified δ-phase peaks. This observation underscores the superior environmental stability of the SCTF prepared with OA. The material's optoelectronic properties are significantly influenced by its defect density.

Hence, we utilized the space-charge-limited current (SCLC) method to compare trap densities of $FA_{0.9}MA_{0.1}PbI_3$ single-crystalline films prepared with OA and Fa as additives, depicted in Fig. 4c, d. The trap density (n) was determined using for-

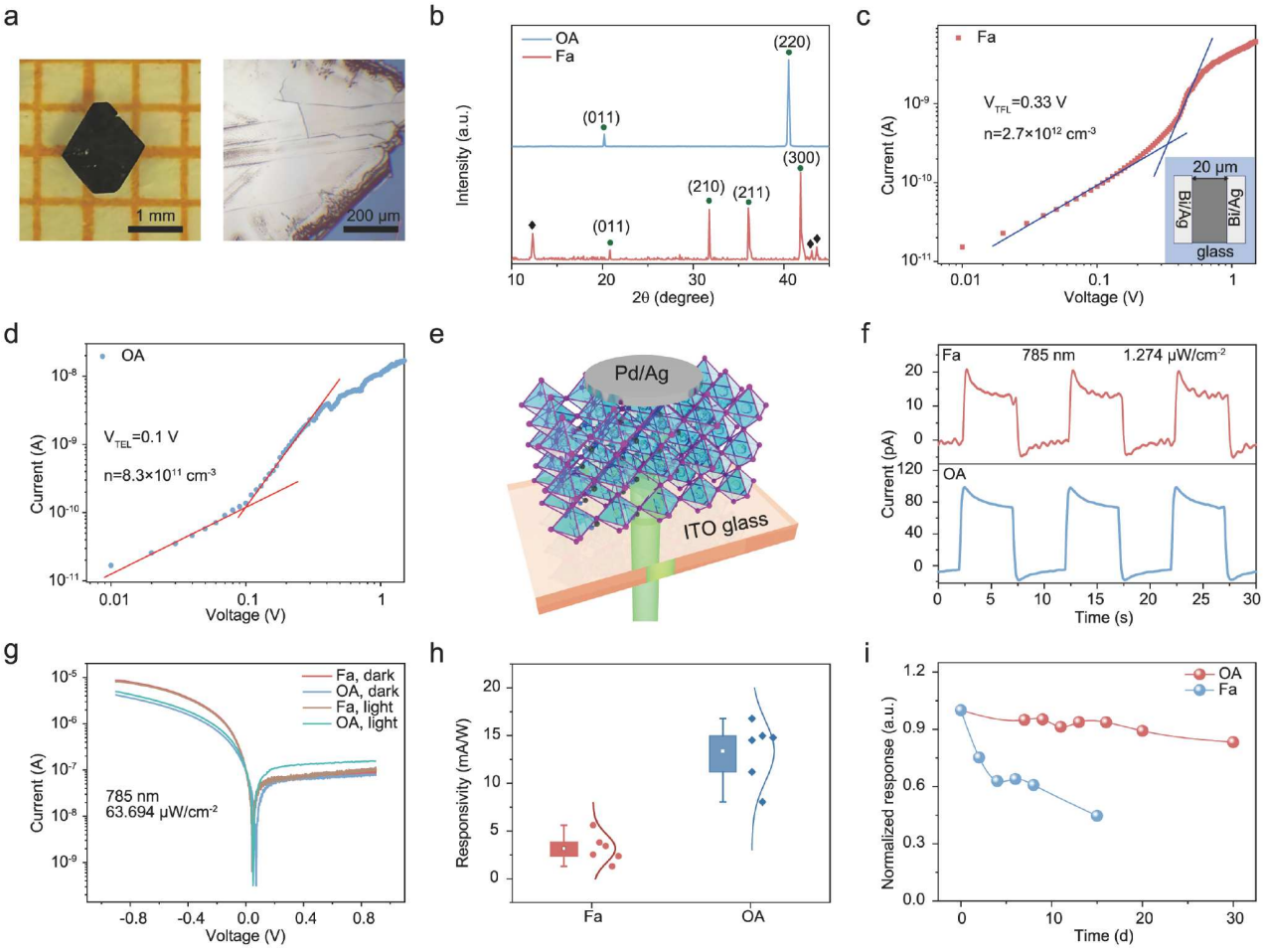

Figure 4 (a) $FA_{0.9}MA_{0.1}PbI_3$ single-crystalline films grown using OA as additive. (b) XRD patterns of single-crystalline films grown with different additives. (c) *I-V* characteristics of FaPD (the inset shows the structure of the electron-only device for SCLC measurement). (d) *I-V* characteristics of OAPD. (e) Schematic diagram of the vertically structured $FA_{0.9}MA_{0.1}PbI_3$-based PD. (f) Spectral response characteristics of OAPD and FaPD under 785 nm laser illumination. (g) *I-V* characteristics of the detectors under dark conditions and 785 nm laser irradiation. (h) Performance statistics of OAPD and FaPD. (i) Long-term stability of unencapsulated PDs stored under ambient conditions for 30 days.

mula (6):

$$n = \frac{2\varepsilon_0\varepsilon_r V_{TFL}}{eL^2}, \quad (6)$$

where L is the electrode spacing, ε_r is the relative dielectric constant of $FA_{0.9}MA_{0.1}PbI_3$, ε_0 is the vacuum permittivity, V_{TFL} is the trap-filling limit voltage, and e is the electron charge.

The trap density of OA-$FA_{0.9}MA_{0.1}PbI_3$ SCTF is merely 8.3 × 10^{11} cm^{-3}, nearly three times lower than that of 2.7 × 10^{12} cm^{-3} for Fa-$FA_{0.9}MA_{0.1}PbI_3$ (Fig. 4c, d). Subsequently, to investigate the optoelectronic properties of the obtained $FA_{0.9}MA_{0.1}PbI_3$ SCTFs, we fabricated vertically structured PDs based on SC films (Ag/Pd/$FA_{0.9}MA_{0.1}PbI_3$/ITO), to investigate the optoelectronic properties of the obtained $FA_{0.9}MA_{0.1}PbI_3$ SCTFs, as detailed in Fig. 4e, and conducted optoelectronic performance tests. The PDs fabricated using OA and Fa as additives are designated as OAPD and FaPD, respectively. The performance characterization and evaluation of photodetectors in this study adhere to recent consensus guidelines rooted in emerging semiconductor technologies, with the aim of accurately assessing photodetector performance [55]. Fig. 4f illustrates the on-off photoresponses of FaPD and OAPD under zero bias when exposed to a 785 nm laser with the same optical power (1.274 μW/cm^2). The OAPD displayed more pronounced pyroelectric current peaks. In Fig. 4g, the current-voltage (*I-V*) characteristics of the devices are depicted under dark conditions and 785 nm laser illumination, showcasing typical rectification and photoresponse behaviors of a p-n junction. Fig. S19 exhibits the on-off photoresponses of FaPD and OAPD detectors at 0 V bias under 785 nm illumination with varying power densities, all revealing distinct transient pyroelectric responses.

As depicted in Fig. S20, all the peak-to-peak current ($I_{pyro+photo}$-$I_{pyro'}$), positive current peak ($I_{pyro+photo}$), and photocurrent (I_{photo}) exhibited a steady increase with rising power density. The OAPD achieved a maximum responsivity (R_I) of 14.5 mA/W and detectivity (D^*) of 3.75 × 10^{10} Jones at the lowest power density of 0.255 μW/cm^2. The FaPD demonstrated a maximum R_I of 2.3 mA/W and D^* of 0.19 × 10^8 Jones (Fig. S21). Table 1 presents a comparison of the photodetection capabilities of our $FA_{0.9}MA_{0.1}PbI_3$-based PD with cutting-edge perovskite photodetectors detailed in recent literature. It is crucial to recognize that factors like responsivity and specific detectivity heavily rely on the applied bias voltage. Our device achieves a responsivity of 14.5 mA/W and a detectivity of 3.75 ×

Table 1 Comparison of reported performance of perovskite PDs

Active materials	Wavelength (nm)	Responsivity (mA/W)	Detectivity (Jones)	Rise time (s)	Decay time (s)	Bias voltage (V)
$MAPbI_3$ [56]	1064	1.6×10^{-3}	1.2×10^{7}	2.8×10^{-5}	3.3×10^{-5}	0
$MAPbI_3$/n-Si [57]	780	3.8	3.4×10^{7}	4×10^{-2}	1.2×10^{-2}	0
$MAPbBr_3$ [58]	530	410	6.39×10^{11}	1.4×10^{-2}	1×10^{-2}	0.95
$FAPbI_3$ [59]	365	860	2.45×10^{9}	6.51	6.9	1
$CsAg_2I_3$ [60]	265	26.5	2.09×10^{8}	0.26	0.29	0
$FAPbBr_{2.5}I_{0.5}$ [61]	580	59.89	–	2×10^{-4}	3.1×10^{-4}	0
$MAPbCl_3$ [62]	377	8	2.93×10^{11}	4×10^{-5}	9.8×10^{-5}	0
$FA_{0.9}MA_{0.1}PbI_3$ (this work)	785	14.5	3.75×10^{10}	1.49×10^{-4}	0.65×10^{-4}	0

10^{10} Jones at zero bias voltage, surpassing or rivaling many devices produced using hazardous solvents like GBL and *N*,*N*-dimethylformamide (DMF). Noteworthy is that this performance is accomplished utilizing an eco-friendly solvent (GVL) and a low-temperature crystallization process, underscoring the efficacy of our solvent-additive synergy approach in facilitating both environmental sustainability and superior optoelectronic performance. The corresponding dark current and noise current are depicted in Fig. S22. The OAPD exhibits quicker response characteristics with a rise time of 149 μs and fall time of 65 μs (Fig. S23).

We methodically assessed the optoelectronic performance of six OAPDs and FAPDs each. Statistical analysis confirmed the OAPD's superior performance compared to its FAPD counterparts (Fig. 4h). Stability assessments revealed that following 30 days of storage under ambient conditions, the device's performance only degraded by 17% (Fig. S24). These outcomes illustrate that the $FA_{0.9}MA_{0.1}PbI_3$ single-crystalline film photodetectors cultivated using GVL and reductive acid additives exhibit exceptional stability.

CONCLUSIONS

This study addresses the instability of the δ-phase in $FAPbI_3$ and the toxicity of solvents by utilizing a sustainable approach. GVL facilitates the formation of stable α-phase crystals (>3 months) at room temperature by forming hydrogen bonds between FA^+ and GVL, along with high-valence $[PbI_x]^{2-x}$ clusters. Additionally, the δ-$FAPbI_3$-GVL intermediate discovered in this study enables the crystallization of the α-phase at low temperatures (60 °C). By incorporating reductive acid additives such as OA, two suppression mechanisms are employed: H^+ enhances the dissociation of FA^+, while reductive group-blocked MA^+ deprotonation eliminates impurities associated with the δ-phase impurities. This methodology results in the production of single-crystalline films of $FA_{0.9}MA_{0.1}PbI_3$ with extremely low defects (8.3×10^{11} cm^{-3}), leading to photodetectors with high responsivity (14.5 mA/W), detectivity (3.75×10^{10} Jones), and environmental durability (83% retention/30 days). The interaction between solvents and additives outlined in this study establishes an environmentally friendly approach for the development of stable perovskite optoelectronic devices on a large scale.

Received 6 December 2025; accepted 22 January 2026; published online 6 May 2026

1 Gao H, Xiao K, Lin R, *et al.* Homogeneous crystallization and buried interface passivation for perovskite tandem solar modules. Science, 2024, 383: 855–859
2 Liu C, Yang Y, Chen H, *et al.* Two-dimensional perovskitoids enhance stability in perovskite solar cells. Nature, 2024, 633: 359–364
3 Wang Y, Lin R, Liu C, *et al.* Homogenized contact in all-perovskite tandems using tailored 2D perovskite. Nature, 2024, 635: 867–873
4 Zhu P, Wang D, Zhang Y, *et al.* Aqueous synthesis of perovskite precursors for highly efficient perovskite solar cells. Science, 2024, 383: 524–531
5 Wei Q, Zhu W, Li T, *et al.* Recent advancements in two-dimensional materials for terahertz photodetectors. Sci China Mater, 2025, 68: 933–946
6 Sidhik S, Metcalf I, Li W, *et al.* Two-dimensional perovskite templates for durable, efficient formamidinium perovskite solar cells. Science, 2024, 384: 1227–1235
7 Liu D, Zheng Y, Sui XY, *et al.* Universal growth of perovskite thin monocrystals from high solute flux for sensitive self-driven X-ray detection. Nat Commun, 2024, 15: 2390
8 Li M, Yang Y, Kuang Z, *et al.* Acceleration of radiative recombination for efficient perovskite LEDs. Nature, 2024, 630: 631–635
9 Tang K, Sha S, Wan P, *et al.* Boosting performances of ZnO microwire homojunction ultraviolet self-powered photodetector by coupled interfacial engineering and plasmonic effects. Sci China Mater, 2024, 67: 842–851
10 Zhou S, Fu S, Wang C, *et al.* Aspartate all-in-one doping strategy enables efficient all-perovskite tandems. Nature, 2023, 624: 69–73
11 Wen B, Chen T, Yin Q, *et al.* Robust chelated lead octahedron surface for efficient and stable perovskite solar cells. Nat Commun, 2024, 15: 7720
12 Lou Q, Xu X, Lv X, *et al.* Room temperature ionic liquid capping layer for high efficiency $FAPbI_3$ perovskite solar cells with long-term stability. Adv Sci, 2024, 11: 2400117
13 Kim H, Yoo SM, Ding B, *et al.* Shallow-level defect passivation by 6H perovskite polytype for highly efficient and stable perovskite solar cells. Nat Commun, 2024, 15: 5632
14 He R, Wang W, Yi Z, *et al.* Improving interface quality for 1-cm^2 all-perovskite tandem solar cells. Nature, 2023, 618: 80–86
15 Liang H, Zhang J, Gao Y, *et al.* Self-powered and charge-transport-layer-free photodetectors based on chloride treated perovskites for weak light detection. Sci China Mater, 2024, 67: 2193–2200
16 Zhang J, Yang Y, Li W, *et al.* Precise arraying of perovskite single crystals through droplet-assisted self-alignment. Sci Adv, 2024, 10: eado0873
17 Wang Y, Shi Z, Wang Y, *et al.* Intermediate phase free α-$FAPbI_3$ perovskite via green solvent assisted perovskite single crystal redissolution strategy. Adv Mater, 2023, 35: 2302298
18 Chu D, Jia B, Liu N, *et al.* Lattice engineering for stabilized black $FAPbI_3$ perovskite single crystals for high-resolution X-ray imaging at the lowest dose. Sci Adv, 2023, 9: 2255
19 Wen J, Zhao Y, Wu P, *et al.* Heterojunction formed via 3D-to-2D perovskite conversion for photostable wide-bandgap perovskite solar cells. Nat Commun, 2023, 14: 7118
20 Liang Y, Li F, Cui X, *et al.* Toward stabilization of formamidinium lead iodide perovskites by defect control and composition engineering. Nat

Commun, 2024, 15: 1707
21 Shi P, Ding Y, Ding B, *et al.* Oriented nucleation in formamidinium perovskite for photovoltaics. Nature, 2023, 620: 323–327
22 Shin S, Seo S, Jeong S, *et al.* Kinetic-controlled crystallization of α-$FAPbI_3$ inducing preferred crystallographic orientation enhances photovoltaic performance. Adv Sci, 2023, 10: 2300798
23 Chen L, Yoo JW, Hu M, *et al.* Intrinsic phase stability and inherent bandgap of formamidinium lead triiodide perovskite single crystals. Angew Chem Int Ed, 2022, 61: e202212700
24 Yin S, Jiao X, Liu X, *et al.* Synergistic effect of H^+ and I^- oxidation enables long-term stability of the precursor solutions and enhanced performance of FA-dominated perovskite solar cells. Adv Funct Mater, 2024, 34: 2411183
25 Bu T, Ono LK, Li J, *et al.* Modulating crystal growth of formamidinium–caesium perovskites for over 200 cm^2 photovoltaic submodules. Nat Energy, 2022, 7: 528–536
26 Chen R, Wang J, Liu Z, *et al.* Reduction of bulk and surface defects in inverted methylammonium- and bromide-free formamidinium perovskite solar cells. Nat Energy, 2023, 8: 839–849
27 Hope MA, Mishra A, Emsley L. Hydrogen diffusion in hybrid perovskites from exchange NMR. Chem Mater, 2024, 36: 7525–7532
28 Lv M, Li N, Jin G, *et al.* Phase-stable $FAPbI_3$-based single crystals with 600-μm electron diffusion length. Matter, 2023, 6: 4388–4400
29 Xing J, Sun Y, He S, *et al.* Triple-cation mixed-halide perovskite single-crystal thin-film for high-performance photodetector via adjusting lattice strain and mitigating surface defects. Adv Funct Mater, 2024, 34: 2411619
30 Zhang L, Luo G, Zhang W, *et al.* Strain regulation and defect passivation of FA-based perovskite materials for highly efficient solar cells. Adv Sci, 2024, 11: 2305582
31 Gao W, Ding J, Ma Q, *et al.* Synergistic modulation of orientation and steric hindrance induced by alkyl chain length in ammonium salt passivator toward high-performance inverted perovskite solar cells and modules. Adv Mater, 2024, 37: 2413304
32 Huang Z, Bai Y, Huang X, *et al.* Anion–π interactions suppress phase impurities in $FAPbI_3$ solar cells. Nature, 2023, 623: 531–537
33 Li M, Sun R, Chang J, *et al.* Orientated crystallization of FA-based perovskite via hydrogen-bonded polymer network for efficient and stable solar cells. Nat Commun, 2023, 14: 573
34 Liu Y, Zhang Y, Zhu X, *et al.* Inch-sized high-quality perovskite single crystals by suppressing phase segregation for light-powered integrated circuits. Sci Adv, 2021, 7: 8844
35 Meng H, Mao K, Cai F, *et al.* Inhibition of halide oxidation and deprotonation of organic cations with dimethylammonium formate for air-processed p–i–n perovskite solar cells. Nat Energy, 2024, 9: 536–547
36 Satale VV, Chowdhury S, Mohamed A, *et al.* Green solvent enabled perovskite ink for ambient-air-processed efficient inkjet-printed perovskite solar cells. Adv Funct Mater, 2025, 35: 40
37 Song Z, Zou Y, Gao Y, *et al.* Buried and bulk synergistic engineering enables high-performance inverted 2D/3D perovskite solar cells. Energy Environ Sci, 2025, 18: 3740–3749
38 Wang Q, Xiong J, Xing Y, *et al.* Reductive Sn^{2+} compensator for efficient and stable Sn-Pb mixed perovskite solar cells. Adv Sci, 2024, 11: 2400962
39 Jeong J, Kim M, Seo J, *et al.* Pseudo-halide anion engineering for α-$FAPbI_3$ perovskite solar cells. Nature, 2021, 592: 381–385
40 Huang L, Wang B, Shuai Q, *et al.* Funnel-shaped precursor engineering for high-performance flexible perovskite photodetectors. Sci China Mater, 2025, 68: 2308–2316
41 Xing R, Li Z, Zhao W, *et al.* Waterproof and flexible perovskite photodetector enabled by p-type organic molecular rubrene with high moisture and mechanical stability. Adv Mater, 2024, 36: 2310248
42 Li Z, Sun S, Jiang H, *et al.* γ-Valerolactone enabling spontaneously inhibited iodide oxidation for high-quality perovskite single crystal fabrication. Adv Funct Mater, 2024, 34: 2407629
43 Liu X, Jiao X, Yin S, *et al.* Oxidization strategy of coordinating solvents mitigates composition segregation in perovskite. Nano Energy, 2025, 136: 110717
44 Moazzezi P, Yeddu V, Cheong IT, *et al.* Discovery of perovskite cosolvency and undoped $FAPbI_3$ single-crystal solar cells fabricated in ambient air. J Am Chem Soc, 2025, 147: 10203–10211
45 Cao J, Zhan W, Ren M, *et al.* High-brightness perovskite light-emitting diodes with suppressed efficiency roll-off using the green solvent γ-valerolactone. ACS Nano, 2025, 19: 9053–9060
46 Chu D, Liu N, Xie S, *et al.* Stable and ultrasensitive X-ray detectors based on oriented single-crystal perovskite rods. Adv Mater, 2025, 37: 2500101
47 Hyun Park S, Su Jin I, Woong Jung J. Green solvent engineering for environment-friendly fabrication of high-performance perovskite solar cells. Chem Eng J, 2021, 425: 131475
48 Meng F, Cheng L, Wang F, *et al.* Sustainable green solvents for lead halide perovskites. Adv Sustain Syst, 2024, 9: 2400695
49 Miao Y, Ren M, Chen Y, *et al.* Green solvent enabled scalable processing of perovskite solar cells with high efficiency. Nat Sustain, 2023, 6: 1465–1473
50 Nambiraj B, Kunka Ravindran A, Muthu SP, *et al.* Cost-effective synthesis method: toxic solvent-free approach for stable mixed cation perovskite powders in photovoltaic applications. Small Methods, 2024, 9: 2400768
51 Huang X, Deng G, Zhan S, *et al.* Solvent gaming chemistry to control the quality of halide perovskite thin films for photovoltaics. ACS Cent Sci, 2022, 8: 1008–1016
52 Chen L, Hu M, Lee S, *et al.* Deciphering reaction products in formamidine-based perovskites with methylammonium chloride additive. J Am Chem Soc, 2023, 145: 27900–27910
53 Chen L, Hu M, Risqi AM, *et al.* Unraveling the influence of solvent on side reactions between formamidinium lead triiodide and methylammonium cations. J Am Chem Soc, 2024, 146: 10159–10166
54 Gou Y, Dai W, Xie X, *et al.* Suppressing deprotonation to extend the shelf life of perovskite precursor solutions and enhance the stability and efficiency of perovskite solar cells. Adv Funct Mater, 2025, 35: 2505965
55 Pecunia V, Anthopoulos TD, Armin A, *et al.* Guidelines for accurate evaluation of photodetectors based on emerging semiconductor technologies. Nat Photon, 2025, 19: 1178–1188
56 Li Y, Zhang Y, Li T, *et al.* A fast response, self-powered and room temperature near infrared-terahertz photodetector based on a $MAPbI_3$/PEDOT:PSS composite. J Mater Chem C, 2020, 8: 12148–12154
57 Yang Z, Wang H, Guo L, *et al.* A self-powered photodetector based on $MAPbI_3$ single-crystal film/n-Si heterojunction with broadband response enhanced by pyro-phototronic and piezo-phototronic effects. Small, 2021, 17: 2101572
58 Anilkumar V, Mahapatra A, Nawrocki J, *et al.* Metal-doped $MAPbBr_3$ single crystal p-n junction photodiode for self-powered photodetection. Adv Opt Mater, 2023, 12: 2302032
59 Shen J, Yu X, Tu W. Multifunctional and high-performance $FAPBI_3$ quantum dots/graphene UV photodetectors by the modulation of photoconductivity. Adv Opt Mater, 2023, 11: 2300410
60 Zhang M, Yan J, Ma J, *et al.* High-quality $CsAg_2I_3$ microwires grown by spatial confinement method for self-powered UV photodetectors. Adv Opt Mater, 2023, 11: 2203054
61 Liang F, Zhou L, Hu Y, *et al.* Self-driven narrow-band photodetector based on $FAPbBr_{2.5}I_{0.5}$ single crystal for yellow light intensity meter application. Adv Funct Mater, 2023, 33: 2302175
62 Wang Z, Zhang X, Wu J, *et al.* Utilizing angle-dependent photovoltage effect in a $CH_3NH_3PbCl_3$/Si heterojunction toward high-performance polarized light detection in ultraviolet region. Adv Opt Mater, 2023, 11: 2202383

Acknowledgement This work was supported by the National Natural Science Foundation of China (52472158, 52125205, 12474401), the Science and Technology Plan Project of Hebei Province (226Z1002G), the Natural Science Foundation of Hebei Province (E2025201007), the Research Innovation Team Project of Hebei University (IT2023A04), and the Interdisciplinary Research Program of Natural Science of Hebei University (DXK202304).

Author contributions Yang Z and Guo L conceived this study and provided supervision for the project. Guo M performed the experimental work

with the assistance of Yang Z and Guo L. Wang Y, Zhang B, Huang H, and Li S were responsible for the testing and calculation of the crystal structure. Wang Z performed the dynamic light scattering measurements. Guo M drafted the manuscript with support from Yang Z. Yang Z and Guo L revised it. The remaining authors assisted in analyzing the experimental results, contributed to the theoretical analysis, and revised the manuscript. All authors reviewed the final manuscript.

Conflict of interest The authors declare that they have no conflict of interest.

Supplementary information Supplementary materials are available in the online version of the paper.

Meitong Guo is currently a graduate student at the College of Physical Science and Technology, Hebei University. Her current research focuses on pyroelectric photodetectors based on formamidinium perovskite single crystals and thin films prepared with green solvents.

Zheng Yang received his PhD degree in nanoscience and nanotechnology from the Beijing Institute of Nanoenergy and Nanosystems, Chinese Academy of Sciences in 2019. Now he is an associate professor in the College of Physics Science and Technology, Hebei University. His research is mainly focused on the research on photodetectors based on the optoelectronic-photothermal coupling effect.

绿色溶剂工程与添加剂调控构筑稳定黑相$FAPbI_3$钙钛矿单晶用于高性能光电探测器

郭美彤[1†], 王颖[2†*], 周斌艺[1], 李思雨[2], 张兵兵[2], 黄鸿博[2], 王振光[2], 李磊朋[1,3*], 王淑芳[1], 郭林娟[1], 潘曹峰[4*], 杨政[1,3*]

摘要 甲脒铅基钙钛矿($FAPbI_3$)因其优异的性能, 在光电子领域具有巨大的应用潜力. 然而, $FAPbI_3$钙钛矿面临着δ相稳定性不足以及制备过程依赖有毒溶剂的双重挑战. 本研究提出一种绿色溶剂-添加剂协同策略, 采用γ-戊内酯(GVL)与功能性添加剂(如草酸等还原性酸)联用的方式, 实现α相$FAPbI_3$单晶的稳定制备. GVL可通过形成FA^+-GVL氢键与高价态的$[PbI_x]^{2-x}$, 提升前驱体的稳定性, 最终可获得在室温环境下稳定存在的α相单晶. 相较于以有毒溶剂γ-丁内酯(GBL)制备的单晶, 该方法制备的材料在稳定性方面实现了显著提升. 添加剂调控实验表明, H^+与还原性基团在调控晶体生长过程中发挥关键作用, 二者可通过促进FA^+解离、抑制MA^+去质子化的方式实现对δ相的有效抑制. 研究中, 我们发现了一种溶剂参与型中间体δ-$FAPbI_3$-GVL, 该中间体可在60 °C的低温条件下转化为α-$FAPbI_3$, 降低α相与δ相间的相变能垒. 与之相反, 乙酸等非还原性酸以及甲酸甲胺等还原性离子液体均无法抑制δ相的生成, 后者甚至会促进纯δ相甲脒铅碘钙钛矿的结晶. 本研究选用低挥发性草酸作为添加剂, 所制备的优化后的$FA_{0.9}MA_{0.1}PbI_3$单晶薄膜缺陷密度低至8.3×10^{11} cm^{-3}. 基于该优化后的单晶薄膜, 我们制备了光电探测器器件. 其在零偏压780 nm光照条件下, 器件的响应度达14.5 mA/W, 探测率为3.75×10^{10} Jones, 响应速度为149/65 μs. 此外, 该器件在无任何封装的情况下, 于室温环境中存放30天后性能仅衰减17%, 展现出优异的稳定性.